SU(4) Heisenberg model on the honeycomb lattice with exchange-frustrated perturbations: Implications for twistronics and Mott insulators

W. M. H. Natori [1,2] R. Nutakki,[3] R. G. Pereira,[4] and E. C. Andrade [1]

[1]*Instituto de Física de São Carlos, Universidade de São Paulo, São Carlos, São Paulo 13560-970, CP 369, Brazil*
[2]*Blackett Laboratory, Imperial College London, London SW7 2AZ, United Kingdom*
[3]*Department of Physics, University of Bath, Claverton Down, Bath BA2 7AY, United Kingdom*
[4]*International Institute of Physics and Departamento de Física Teórica e Experimental, Universidade Federal do Rio Grande do Norte, Natal, Rio Grande do Norte, 59078-970, Brazil*

The SU(4)-symmetric spin-orbital model on the honeycomb lattice was recently studied in connection to correlated insulators such as the e_g Mott insulator $Ba_3CuSb_2O_9$ and the insulating phase of magic-angle twisted bilayer graphene at quarter filling. Here we provide a unified discussion of these systems by investigating an extended model that includes the effects of Hund's coupling and anisotropic, orbital-dependent exchange interactions. Using a combination of mean-field theory, linear flavor-wave theory, and variational Monte Carlo, we show that this model harbors a quantum spin-orbital liquid over a wide parameter regime around the SU(4)-symmetric point. For large Hund's coupling, a ferromagnetic antiferro-orbital ordered state appears, while a valence-bond crystal combined with a vortex orbital state is stabilized by dominant orbital-dependent exchange interactions.

I. INTRODUCTION

Kugel-Khomskii (KK) models [1] are effective Hamiltonians with couplings between spin and orbital degrees of freedom that describe various phenomena in transition metal oxides [2,3]. Recently, the applications of KK models have been extended to Mott insulators with strong spin-orbit coupling [4], iron-pnictide superconductors [5], Coulomb impurity lattices designed with scanning tunneling microscope [6], and cold atom systems [7]. In realistic KK models, the interplay between orbital configuration and lattice geometry generally constrains the virtual electron transfers and generates exchange frustration in the form of bond-dependent and anisotropic spin-orbital interactions [4]. This kind of exchange enhances quantum fluctuations even in unfrustrated lattices [8], leading to the expectation that KK models may present exotic orders, valence bond crystals (VBCs), or even quantum spin-orbital liquids (QSOLs) as their ground states [9].

The most well-studied examples of KK models display two-orbital degeneracy and can be implemented in three distinct solid-state platforms. Historically, the first one arises in Mott insulators with e_g orbitals [1], where the orbital Hilbert space is spanned by $d_{3z^2-r^2}$ and $d_{x^2-y^2}$ orbitals [10–14]. The second platform comprises t_{2g} Mott insulators with $4/5d^1$ magnetic species, in which the strong spin-orbit coupling (SOC) favors a low-energy $j = 3/2$ multiplet [15]. These models can be alternatively expressed in terms of pseudospins and pseudo-orbitals that mimic the e_g operators [16–20]. Lastly, two-orbital degenerate KK models were proposed as relevant descriptions for correlated insulators observed in twistronic systems [21,22]. This proposal hangs upon the

validity of Wannier orbitals to reproduce the twist-induced flat bands. If this is the case and the interactions are sizable enough to describe these systems in the strong-coupling regime, then KK Hamiltonians naturally arise as minimal models for their insulating phases [23–30].

One example of the two-orbital KK model is the SU(4) Heisenberg model, which is receiving renewed interest due to suggested implementations in the three solid-state platforms described above [19,20,23–32]. Although the model is not exchange-frustrated, the higher symmetry fosters liquid ground states as first noted in SU(N) "spin" models in the large-N limit [33–35]. A specific study of the SU(4) Heisenberg model on the honeycomb lattice was performed in Ref. [36] using several numerical and analytical techniques. The combination of exact diagonalization (ED) and variational Monte Carlo (VMC) provided good evidence in favor of a π-flux QSOL with fermionic excitations similar to the ones obtained in large-N theories. The experimental motivation of the authors of Ref. [36] was the e_g system $Ba_3CuSb_2O_9$, in which Cu^{2+} ions were proposed to form layered honeycomb lattices [37]. Other theoretical descriptions of the same compound also regarded the SU(4) Heisenberg model as relevant, but included exchange-frustrated terms induced by orbital-dependent virtual hopping processes [31,38]. In the last year, two new platforms for the SU(4) Heisenberg model were proposed: the analogues of Kitaev materials with $4/5d^1$ magnetic species (e.g., α-ZrCl$_3$) [19,20] and the Mott phase of twisted bilayer graphene (TBG) [24].

The purpose of this paper is to study the effects of exchange-frustrated and Hund's coupling induced interactions on the SU(4) Heisenberg model on the honeycomb lattice. We present a detailed analysis of a KK model derived
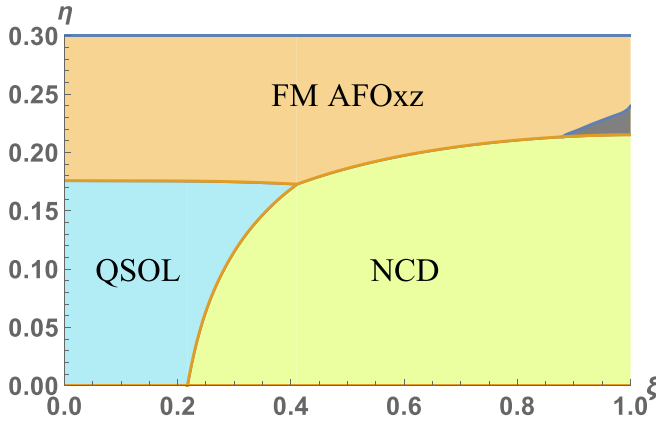
FIG. 1. Phase diagram of the Kugel-Khomskii model as a function of the ratio of hopping parameters $\xi = t'/t$ and the dimensionless Hund's coupling parameter $\eta = J_H/U$. There are three distinct phases: a quantum spin-orbital liquid (QSOL, in blue), a noncollinear ordering of spin dimers (NCD, in green), and a ferromagnetic state with staggered orbital order (FM AFOxz, in orange). A region of instability of the last phase is indicated in gray and discussed in Sec. III B.

independently in Refs. [24] and [31] using mean-field theory (MFT), linear flavor-wave theory (LFWT) (complemented by a variational study considering the Huse-Elser wave function [39,40]), and VMC. Our main results are summarized in Fig. 1. Our study corroborates the existence of a stable QSOL phase around the SU(4)-symmetric point studied in Ref. [36]. For larger values of the SU(4)-symmetry-breaking interactions, we find either a two-sublattice state with ferromagnetic order for the spin degrees of freedom or a VBC phase of spin dimers coupled to a three-sublattice vortex orbital state. Our phase diagram agrees qualitatively with the one obtained by the authors of Ref. [31] by exact diagonalization of the same model on small clusters.

The remaining sections are organized as follows. We present the local degrees of freedom and the KK model in Sec. II. Besides fixing the notation, this section also discusses the properties of the orbital degrees of freedom and symmetries of the model that will be relevant for our subsequent analysis. Section III identifies possible ordered ground states of the KK model using MFT, expanding the phase diagram presented in Ref. [24]. The effects of quantum fluctuations on these states are then evaluated within LFWT. The QSOL proposed in Ref. [36] and possible VBCs ground states of this KK model are studied within VMC as presented in Sec. IV. The phase diagram in Fig. 1 is constructed through the combination of the LFWT and VMC energetics studies. The relevance of our results and perspectives for future work are provided in Sec. V.

II. MICROSCOPIC MODELS

A. Local degrees of freedom

Let us start with a brief description of the local degrees of freedom of the magnetic species that we are investigating. We assign to each site a spin 1/2 as well as an orbital degree of freedom corresponding to quantum numbers $S^z = \pm\frac{1}{2}$ and

$\tau^z = \pm\frac{1}{2}$, respectively. The Hilbert space of each site i is then spanned by four states $|S_i^z, \tau_i^z\rangle$ (often called *colors*) which are labeled as

$$|1\rangle = \left|\tfrac{1}{2}, \tfrac{1}{2}\right\rangle, \quad |2\rangle = \left|-\tfrac{1}{2}, \tfrac{1}{2}\right\rangle,$$
$$|3\rangle = \left|\tfrac{1}{2}, -\tfrac{1}{2}\right\rangle, \quad |4\rangle = \left|-\tfrac{1}{2}, -\tfrac{1}{2}\right\rangle. \quad (1)$$

The operators for spin ($\mathbf{S}_i$) and orbital ($\boldsymbol{\tau}_i$) obey the usual SU(2) algebra $[S_i^\alpha, S_j^\beta] = i\epsilon^{\alpha\beta\gamma} S_i^\gamma \delta_{ij}$, $[\tau_i^\alpha, \tau_j^\beta] = i\epsilon^{\alpha\beta\gamma} \tau_i^\gamma \delta_{ij}$ and $[S_i^\alpha, \tau_j^\beta] = 0$ and are represented by the Pauli matrices in their respective spaces.

The orbital degree of freedom may describe, for instance, a low-energy e_g doublet $\{d_{3z^2-r^2}, d_{x^2-y^2}\}$ in Mott insulators with octahedral crystal field [4]. Alternatively, it may refer to p_x and p_y orbitals in optical lattices [41] or twistronic systems [24]. The doublets in these two cases constitute the orthogonal eigenstates of the τ^z operator. We will be concerned only with Hamiltonians that remain invariant under C_3 rotations around the normal axis of the honeycomb lattice. Similar C_3 rotations on the internal orbital subspace spanned by (τ^z, τ^x) accounts for the effect of the spatial transformations on the orbitals. The remaining component τ^y has a distinct role that is more easily seen by the effect of the time-reversal operator Θ. In the orbital space, Θ reduces to a complex conjugation and leads to $\Theta\boldsymbol{\tau}\Theta^{-1} = (\tau^x, -\tau^y, \tau^z)$. The physical interpretation of τ^y is that it distinguishes between states with different orbital chiralities [25] and is, therefore, related to orbital-magnetic orders [24].

B. Kugel-Khomskii model

We now introduce the minimal model proposed for the Mott insulating phase of $Ba_3CuSb_2O_9$ and TBG in Refs. [24,31]. Despite the different nature of the orbitals in these systems, their in-plane symmetries enable one to assign the same Hubbard model in both cases. The interactions H_I are restricted to be onsite

$$H_I = U \sum_i \sum_{\alpha=1,2} n_{i,\alpha,\uparrow} n_{i,\alpha,\downarrow} + (U - 2J_H) \sum_i n_{i,1} n_{i,2}$$
$$+ J_H \sum_{i,s,s'} c_{i,1,s}^\dagger c_{i,2,s'}^\dagger c_{i,1,s'} c_{i,2,s}$$
$$+ J_H \sum_{i,\alpha\neq\beta} c_{i,\alpha,\uparrow}^\dagger c_{i,\alpha,\downarrow}^\dagger c_{i,\beta,\downarrow} c_{i,\beta,\uparrow}, \quad (2)$$

in which $c_{i,\alpha,s} = c_{\alpha,s}(\mathbf{r}_i)$ is the annihilation operator of an electron at position $\mathbf{r}_i$ on the honeycomb lattice with orbital state $\alpha = 1, 2$ (corresponding to $\tau^z = \pm\frac{1}{2}$, respectively) and spin $s = \uparrow, \downarrow$ (for $S^z = \pm\frac{1}{2}$). We also introduce the number operator for a given orbital as $n_{i,\alpha} = \sum_s c_{i,\alpha,s}^\dagger c_{i,\alpha,s}$ and two parameters for electrostatic interactions: the direct Coulomb repulsion $U > 0$ and Hund's coupling $J_H > 0$. The tunneling between nearest neighbors on the honeycomb lattice is modeled by the tight-binding Hamiltonian

$$H_{TB} = \sum_{i\in A} \sum_{\alpha,\beta} \sum_{\gamma=1}^3 \sum_s c_{\alpha,s}^\dagger(\mathbf{r}_i) \hat{h}_{\alpha\beta}^{(\gamma)} c_{\beta,s}\left(\mathbf{r}_i + \frac{\hat{\mathbf{e}}_\gamma}{\sqrt{3}}\right) + \text{H.c.}, \quad (3)$$

where $\hat{\mathbf{e}}_1 = \hat{\mathbf{z}}$, $\hat{\mathbf{e}}_2 = -\frac{1}{2}\hat{\mathbf{z}} + \frac{\sqrt{3}}{2}\hat{\mathbf{x}}$, $\hat{\mathbf{e}}_3 = -\frac{1}{2}\hat{\mathbf{z}} - \frac{\sqrt{3}}{2}\hat{\mathbf{x}}$ are unit vectors in the zx plane, and i runs over the A sublattice, i.e., the triangular Bravais lattice. Here we set the lattice spacing of the honeycomb lattice to 1. The matrix $\hat{h}_{\alpha\beta}^{(\gamma)}$ depends on the overlap between the orbitals at positions $\mathbf{r}_i$ and $\mathbf{r}_j$, connected by a link in the direction $\mathbf{r}_{ij} = \mathbf{r}_j - \mathbf{r}_i = \frac{1}{\sqrt{3}}\hat{\mathbf{e}}_\gamma$. Using an analogy with organic chemistry, we can think of two types of hoppings involving p orbitals that are connected by σ or π bonds, as indicated in Fig. 2. The matrix $\hat{h}_{\alpha\beta}^{(\gamma)}$ is then parameterized as [24,31]

$$\hat{h}_{\alpha\beta}^{(\gamma)} = t + 2t'\hat{\mathbf{e}}_\gamma \cdot \boldsymbol{\tau} = \left[t_\sigma\left(\tfrac{1}{2} + \hat{\mathbf{e}}_\gamma \cdot \boldsymbol{\tau}\right) + t_\pi\left(\tfrac{1}{2} - \hat{\mathbf{e}}_\gamma \cdot \boldsymbol{\tau}\right)\right], \tag{4}$$

where $t_{\sigma,\pi} \equiv t \pm t'$.

The KK model derived within second-order perturbation theory in the regime $t, t' \ll U, J_H$ reads

$$\mathcal{H}(\xi, \eta) = \sum_{\langle ij \rangle} \Big\{ J_1 \mathcal{P}_{ij}^1 [(1 - \xi^2)\mathcal{Q}_{ij}^+ - 2(1 + \xi^2)(\mathcal{P}_{ij}^{+-} + \mathcal{P}_{ij}^{-+})]$$

$$- J_2 \mathcal{P}_{ij}^0 \big[8(1 - \xi^2)\tau_i^y \tau_j^y + 2(1 + \xi)^2 \mathcal{P}_{ij}^{++} + 2(1 - \xi)^2 \mathcal{P}_{ij}^{--} + 2(1 + \xi^2)(\mathcal{P}_{ij}^{+-} + \mathcal{P}_{ij}^{-+})\big]$$

$$- J_3 \mathcal{P}_{ij}^0 ((1 - \xi^2)\mathcal{Q}_{ij}^- + 2(1 + \xi)^2 \mathcal{P}_{ij}^{++} + 2(1 - \xi)^2 \mathcal{P}_{ij}^{--}) \Big\}. \tag{5}$$

Here we defined the dimensionless parameters $\xi = t'/t$ and $\eta = J_H/U$ and the exchange coupling constants $J_1 = \frac{J}{1-3\eta}$, $J_2 = \frac{J}{1-\eta}$, $J_3 = \frac{J}{1+\eta}$, where $J = t^2/U$. As usual in KK models, the spin part of the interaction between the electrons at sites i and j is written in terms of the projectors onto states with total spin $S = 0$ and $S = 1$:

$$\mathcal{P}_{ij}^0 = \tfrac{1}{4} - \mathbf{S}_i \cdot \mathbf{S}_j, \quad \mathcal{P}_{ij}^1 = \mathbf{S}_i \cdot \mathbf{S}_j + \tfrac{3}{4}. \tag{6}$$

Notice that the Hamiltonian is invariant under global spin SU(2) rotations. In contrast, the orbital part of the interaction is in general anisotropic and bond dependent, as it involves the operators

$$\mathcal{P}_{ij}^{\mu\nu} \equiv \left(\tfrac{1}{2} + \mu\hat{\mathbf{e}}_{ij} \cdot \boldsymbol{\tau}_i\right)\left(\tfrac{1}{2} + \nu\hat{\mathbf{e}}_{ij} \cdot \boldsymbol{\tau}_j\right), \quad \mathcal{Q}_{ij}^+ = 4[\boldsymbol{\tau}_i \cdot \boldsymbol{\tau}_j - (\hat{\mathbf{e}}_{ij} \cdot \boldsymbol{\tau}_i)(\hat{\mathbf{e}}_{ij} \cdot \boldsymbol{\tau}_j)],$$

$$\mathcal{Q}_{ij}^- = 4\big[\boldsymbol{\tau}_i \cdot \boldsymbol{\tau}_j - 2\tau_i^y \tau_j^y - (\hat{\mathbf{e}}_{ij} \cdot \boldsymbol{\tau}_i)(\hat{\mathbf{e}}_{ij} \cdot \boldsymbol{\tau}_j)\big], \tag{7}$$

where $\mu, \nu \in \{+, -\}$ and $\hat{\mathbf{e}}_{ij} = \hat{\mathbf{e}}_\gamma$ for $\mathbf{r}_{ij} \parallel \hat{\mathbf{e}}_\gamma$. Explicitly, we can write the Hamiltonian as

$$\mathcal{H}(\xi, \eta) = \sum_{\langle ij \rangle} \Bigg\{ (J_1 + J_2)(1 - \xi^2)\left(2\mathbf{S}_i \cdot \mathbf{S}_j + \frac{1}{2}\right)\left(2\boldsymbol{\tau}_i \cdot \boldsymbol{\tau}_j + \frac{1}{2}\right) + (J_1 - J_3)(1 - \xi^2)\left(2\boldsymbol{\tau}_i \cdot \boldsymbol{\tau}_j + \frac{1}{2}\right)$$

$$+ 2(J_2 - J_3)(1 - \xi^2)\left(2\mathbf{S}_i \cdot \mathbf{S}_j - \frac{1}{2}\right)\left(2\tau_i^y \tau_j^y + \frac{1}{2}\right) - (J_1 - 2\xi^2 J_2 - J_3)\left(2\mathbf{S}_i \cdot \mathbf{S}_j + \frac{1}{2}\right)$$

$$+ \xi(J_2 + J_3)4\mathbf{S}_i \cdot \mathbf{S}_j(\hat{\mathbf{e}}_{ij} \cdot \boldsymbol{\tau}_i + \hat{\mathbf{e}}_{ij} \cdot \boldsymbol{\tau}_j) + \xi^2(J_1 + J_3)8\mathbf{S}_i \cdot \mathbf{S}_j(\hat{\mathbf{e}}_{ij} \cdot \boldsymbol{\tau}_i)(\hat{\mathbf{e}}_{ij} \cdot \boldsymbol{\tau}_j)$$

$$+ 2\xi^2(3J_1 - J_3)(\hat{\mathbf{e}}_{ij} \cdot \boldsymbol{\tau}_i)(\hat{\mathbf{e}}_{ij} \cdot \boldsymbol{\tau}_j) - (J_1 + 2\xi^2 J_2 + J_3) \Bigg\}. \tag{8}$$

Let us first consider the model with $\xi = \eta = 0$. In this case, the original two-orbital Hubbard model in Eqs. (2) and (3) is invariant under global SU(4) color transformations. As a result, at this point the KK model reduces to $\mathcal{H}(0, 0) = \mathcal{H}_{\mathrm{SU(4)}} - 3NJ$, where N is the number of sites of the honeycomb lattice and $\mathcal{H}_{\mathrm{SU(4)}}$ is the SU(4) Heisenberg model given by

$$\mathcal{H}_{\mathrm{SU(4)}} = 2J\sum_{\langle ij \rangle}\left(2\mathbf{S}_i \cdot \mathbf{S}_j + \frac{1}{2}\right)\left(2\boldsymbol{\tau}_i \cdot \boldsymbol{\tau}_j + \frac{1}{2}\right),$$

$$= 2J\sum_{\langle ij \rangle}\sum_{a,b=1}^{4} S_a^b(i)S_b^a(j). \tag{9}$$

Here we introduce the color exchange operators

$$S_a^b(i) = |a\rangle_i\langle b|_i, \tag{10}$$

which can be recognized as the SU(4) generators [36]. Any local spin-orbital operator that appears in Eq. (5) can be written as a linear combination of $S_a^b(i)$ operators. In particular, $\mathcal{H}_{\mathrm{SU(4)}}$ is proportional to the sum of color permutation operators $P_{ij} \equiv \sum_{a,b} S_a^b(i)S_b^a(j)$ over all nearest-neighbor bonds.

In the case of isotropic hopping ($\xi = 0$) but nonzero Hund's coupling ($\eta > 0$), the Hamiltonian is given by

$$\mathcal{H}(0, \eta) = \sum_{\langle ij \rangle}\Bigg[4J_1 \mathcal{P}_{ij}^1\left(\boldsymbol{\tau}_i \cdot \boldsymbol{\tau}_j - \frac{1}{4}\right)$$

$$- 8J_2 \mathcal{P}_{ij}^0\left(\tau_i^y \tau_j^y + \frac{1}{4}\right)$$

$$- 4J_3 \mathcal{P}_{ij}^0\left(\boldsymbol{\tau}_i \cdot \boldsymbol{\tau}_j - 2\tau_i^y \tau_j^y + \frac{1}{4}\right)\Bigg]. \tag{11}$$

Thus, along the $\xi = 0$ line in parameter space, the model retains an SU(2)×U(1) symmetry. The U(1) symmetry is due
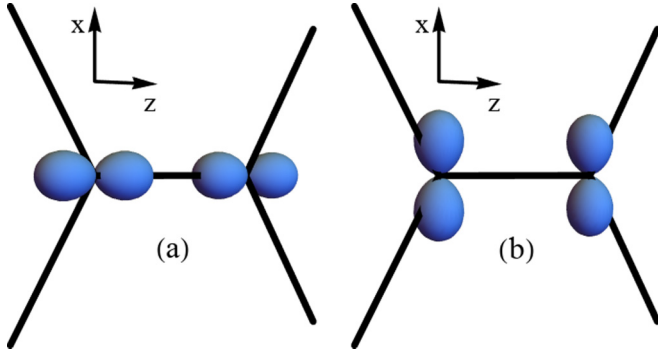
FIG. 2. Representation of (a) p_z and (b) p_x orbitals in the zx plane. The orbitals in (a) overlap with each other analogously to a σ-bond in organic chemistry. Analogously, (b) depicts active orbitals similar to a π-bond.

to the conservation of the orbital chirality, as $\sum_i \tau_i^y$ commutes with the Hamiltonian.

For general values of ξ and η, model (5) exhibits a global SU(2)$\times\mathbb{Z}_3$ symmetry, where the $\mathbb{Z}_3$ symmetry is associated with $\pm 120°$ orbital rotations about τ^y accompanied by the rotation of the bond directions. The bond-dependent hopping t' introduces the exchange-frustrated perturbations given in Eq. (8). Of particular interest are the points $\xi = \pm 1$ with $\eta = 0$, where Eq. (5) becomes

$$\mathcal{H}(\pm 1, 0) = 8J \sum_{\langle ij \rangle} \left(2\mathbf{S}_i \cdot \mathbf{S}_j + \frac{1}{2} \right) \mathcal{P}_{ij}^{++(--)} - 6NJ. \quad (12)$$

The orbital interactions take this form because Eq. (4) involves a projector to either σ or π bonds (Fig. 2). Hence the electrons interact with each other only if they both occupy the orbital state which is an eigenstate of $\hat{\mathbf{e}}_{ij} \cdot \boldsymbol{\tau}$ with eigenvalue $\pm 1/2$ for $t' = \pm t$, respectively. This type of orbital dependence appears in compass models for e_g orbitals [9] or for $j = 3/2$ states after projection of t_{2g} states in the limit of strong spin-orbit coupling [16,17].

III. ORDERED STATES

The first step to gain intuition of the phase diagram of the model in Eq. (5) is to study ordered states with MFT. In this section, we study classical ordered states that are equivalent to a product state

$$|\Psi\rangle = \prod_i |\psi_i\rangle, \quad (13)$$

in which $|\psi_i\rangle$ is a linear combination of the states in Eq. (1). The method provides the phase diagram in Fig. 3(a), which extends the result of Ref. [24] by including nonzero orbital-dependent hopping t'. We shall then analyze the stability of the ordered states against quantum fluctuations using LFWT [42].

A. Mean-field theory

Our choice of ordered states is guided by the symmetries discussed in Sec. II B. The SU(2) symmetry and the absence of geometric frustration suggest that, classically, the spins

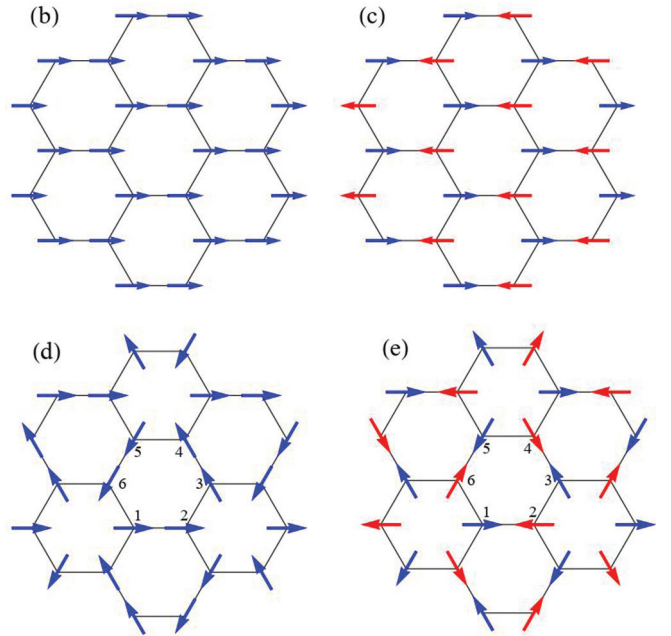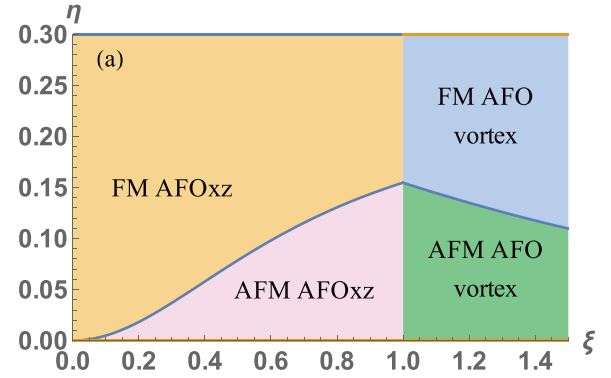FIG. 3. Classical states in the spin-orbit model Eq. (5). (a) Mean-field phase diagram. The spin sector may display ferromagnetic (FM) or antiferromagnetic (AFM) order. In (b) through (d), the arrows represent the orbital order within the plane (τ^z, τ^x): (b) ferro-orbital (FOxz), (c) Néel (AFOxz), (d) ferro-orbital vortex, and (e) antiferro-orbital vortex. The numbers in (d) and (e) indicate the six-sublattice magnetic unit cell.

form either a ferromagnetic (FM) or an antiferromagnetic (AFM) order. Equation (7) suggests that the orbitals may either align with τ^y or be contained in the (τ^z, τ^x) plane. By computing the classical energy for different orbital configurations, we find that only in-plane orbital-ordered states are competitive. When bond-independent interactions dominate, the system develops ferro-orbital (FOxz) or antiferro-orbital (AFOxz) in the xz plane as illustrated in Figs. 3(b) and 3(c). On the other hand, interactions proportional to $(\hat{\mathbf{e}}_{ij} \cdot \boldsymbol{\tau}_i)(\hat{\mathbf{e}}_{ij} \cdot \boldsymbol{\tau}_j)$ favor the "vortex" orbital orders displayed in Figs. 3(d) and 3(e). In fact, the orbital vortex states are the best trial ground states of the compass model on the honeycomb lattice [41]. They also appear as the exact ground state for a special point of the $JK\Gamma$ model for the honeycomb iridates [43].

We find that the mean-field phase diagram is symmetric under $\xi \mapsto -\xi$. Figure 3(a) shows the phase diagram for $\xi > 0$ and $0 < \eta < 0.3$. In the physically more relevant regime $\xi < 1$, we observe a competition between two states with AFOxz order distinguished by the FM or AFM spin order. In agreement with the authors of Ref. [24], the FM state has lower energy for $\xi \to 0$ at any fixed η. The transition from AFOxz to the orbital vortex states across the line $\xi = 1$ can be attributed to a six-sublattice orbital rotation symmetry of the model discussed in Ref. [31], which maps $\mathcal{H}(\xi, \eta) \mapsto \mathcal{H}(1/\xi, \eta)$ and connects the collinear orbital phases in Figs. 3(b) and 3(c) to their vortex counterparts in Figs. 3(d) and 3(e) [43].

B. Linear flavor wave theory

A careful analysis of MFT indicates that the classical phase diagram in Fig. 3(a) is incorrect near the point $\xi = \eta = 0$, corresponding to $\mathcal{H}_{\mathrm{SU(4)}}$. The reason is that the expectation value $\langle \Psi | \mathcal{H}_{\mathrm{SU(4)}} | \Psi \rangle$ is the same for any state in which $\langle \psi_i | \psi_j \rangle = 0$, i.e., whenever neighboring sites have different colors [36]. The number of states satisfying this constraint increases exponentially with the system size and flags the onset of a disordered state. On the other hand, finite Hund's coupling is expected to favor spin ferromagnetism, in consistency with the FM AFOxz phase. It is then desirable to study the effect of quantum fluctuations on the energy and stability of this spin-orbital ordered state.

LFWT can be viewed as the analog of spin wave theory for spin-orbital models [42]. It allows estimates of the excitation dispersion, correction to the zero-point energy and reduction of the order parameter by quantum fluctuations (ΔM) in a single formalism. It also provides some criteria for the stability of a given ordered phase. For example, the application of LFWT to AFM AFOxz leads to dispersion relations with complex frequencies at any $\eta \neq 0$ and $\xi \neq 0$. Such complex dispersion clearly indicates that the AFM AFOxz state is unstable and explains its absence in Fig. 1.

We then study the FM AFOxz state, which is the ordered state with fixed colors $m_A = 3$ and $m_B = 1$ on the A and B sublattices, respectively. The Holstein-Primakoff transformation introduces three bosonic species per sublattice labeled by b_{irm}, in which i indexes the unit cells, r the sublattices and $m \neq m_r$ correspond to the colors in Eq. (1). After replacing spin-orbital operators by their bosonic representations and truncating the Hamiltonian at the level of quadratic terms, the LFWT Hamiltonian is written in the Fourier space as

$$\mathcal{H}_{\mathrm{LFWT}} = -2NJ_1(3 + \xi^2) + \sum_{\mathbf{k}} B_{\mathbf{k}}^{\dagger} \mathcal{H}_{\mathbf{k}} B_{\mathbf{k}}$$
$$- \frac{3}{2}N\left[\left(3 + \frac{\xi^2}{2}\right)J_1 - 2(1 + \xi^2)J_2 - (1 + \xi^2)J_3\right],$$
(14)

where $\mathbf{k}$ lies in the Brillouin zone. Here $B_{\mathbf{k}}^{\dagger}$ is a 12-component spinor containing operators of the form

$$B_{\mathbf{k}}^{\dagger} = \begin{pmatrix} b_{\mathbf{k}A1}^{\dagger} & b_{\mathbf{k}B3}^{\dagger} & b_{-\mathbf{k},A1} & b_{-\mathbf{k},B3} \\ b_{\mathbf{k}A2}^{\dagger} & b_{\mathbf{k}A4}^{\dagger} & b_{\mathbf{k}B2}^{\dagger} & b_{\mathbf{k}B4}^{\dagger} \\ b_{-\mathbf{k},2A} & b_{-\mathbf{k},A4} & b_{-\mathbf{k},B2} & b_{-\mathbf{k},B4} \end{pmatrix},$$
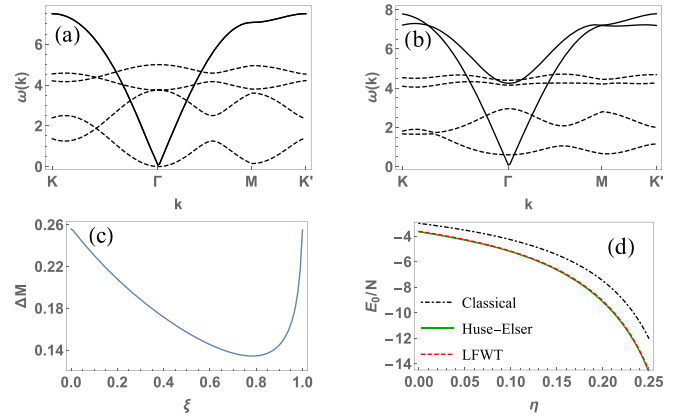(15)

FIG. 4. (a) Dispersions $\omega_{\lambda}(\mathbf{k})$ for $\lambda = 1, 2$ (continuous line) and $\lambda = 3, \ldots, 6$ (dashed lines) of the ordered state FM AFOxz for $\eta = 0.2$ and $\xi = 0$. (b) Dispersions $\omega_{\lambda}(\mathbf{k})$ of the ordered state FM AFOxz for $\eta = 0.2$ and $\xi = 0.4$ with the same convention set in (a). (c) Correction to the order parameter ΔM as a function of ξ for $\eta = 0.2$ (d) Ground-state energy as a function of η at $\xi = 0$ for the FM AFOxz state comparing the classical energy, the LFWT energy, and the Huse-Elser energy.

and $\mathcal{H}_{\mathbf{k}}$ is a 12×12 Hermitian matrix. The ordering of the spinor $B_{\mathbf{k}}^{\dagger}$ is motivated by the fact that bosons of colors $m = 1$ and $m = 3$ are decoupled from bosons with $m = 2$ and $m = 4$. This implies that $\mathcal{H}_{\mathbf{k}}$ can be written in a block diagonal form as

$$\mathcal{H}_{\mathbf{k}} = \begin{pmatrix} \mathcal{H}_{\mathbf{k}}^{(1,3)} & 0 & 0 \\ 0 & \mathcal{H}_{\mathbf{k}}^{(2,4)} & 0 \\ 0 & 0 & \left[\mathcal{H}_{-\mathbf{k}}^{(2,4)}\right]^{*} \end{pmatrix}, \quad (16)$$

in which all the block matrices are 4×4. Diagonalization of the LFWT Hamiltonian gives rise to six flavor dispersions $\omega_{\lambda}(\mathbf{k})$ that will be discussed below. We verify that the flavor waves originated from $\mathcal{H}_{\mathbf{k}}^{(2,4)}$ conserve the total number of bosons, in contrast to what happens for $\mathcal{H}_{\mathbf{k}}^{(1,3)}$. The constant term in the second and third lines of Eq. (14) gets canceled in the diagonalization and do not contribute to the ground-state energy.

Let us now turn to the flavor-wave dispersions $\omega_{\lambda}(\mathbf{k})$ with $\lambda = 1, 2$, which are related to $\mathcal{H}_{\mathbf{k}}^{(1,3)}$. Only the exchange constant J_1 appears in this sector of the LFWT Hamiltonian as a global multiplicative factor. Therefore, the shape of the dispersions $\omega_{\lambda}(\mathbf{k})$ does not vary with η and the bandwidth is directly proportional to J_1. Figure 4(b) shows $\omega_{\lambda}(\mathbf{k})$ for $\xi = 0$ in solid lines. In this case, we observe two degenerate bands with linear dispersion at the Γ point. This degeneracy is lifted by bond-dependent interactions as shown in Fig. 4(b). The resulting band retains a Goldstone mode and another gapped mode.

We now turn to stability criteria given by $\omega_{\lambda}(\mathbf{k})$ with $\lambda = 3, \ldots, 6$ obtained from $\mathcal{H}_{\mathbf{k}}^{(2,4)}$ [see dashed lines in Figs. 4(a) and 4(b)]. First, these bands become zero-energy flat bands in the limit $(\xi, \eta) \to (0, 0)$. This provides another indication of the instability of the ordered state at the SU(4)-symmetric point. Second, $\omega_{\lambda}(\mathbf{k})$ become negative depending on the values of η and t', which provides yet another instability

flag. The region in which this form of instability disrupts an otherwise favored FM AFOxz phase was found numerically and is indicated in gray in Fig. 1. The authors of Ref. [31] also encountered an unidentified phase with ED for small clusters in a close region of the parameter space. LFWT suggests that such phase still exists in the thermodynamic limit, but it is incapable of diagnosing its characteristics. When these bosonic modes display strictly positive frequencies, they do not alter the LFWT ground state. Thus, they do not affect the reduction of the order parameter nor the zero-point energy. The energy of the ordered state calculated with LFWT, E_{LFWT}, considers then only the integration of the modes $\lambda = 1, 2$ and is given by

$$\frac{E_{\text{LFWT}}}{N} = -2J_1\left(3 + \xi^2\right) + \frac{1}{N}\sum_{\mathbf{k}}\sum_{\lambda=1}^{2}\omega_\lambda(\mathbf{k}). \qquad (17)$$

The correction to the order parameter is provided by Fig. 4(c), which shows that $\Delta M \sim 0.14$–0.25 when $\xi < 0.99$. We observe a divergence of ΔM as $\xi \to 1$. This is consistent with the mean-field phase transition occurring at this point due to the six-sublattice mapping discussed above, see Fig. 3. Away from this line, the ordered phase FM AFOxz acquires only mild corrections to the order parameter.

To further check the feasibility of the LFWT energies, we also construct a variational wave function for the ordered FM AFOxz phase, along the line $\xi = 0$, following the proposal by Huse and Elser [39]. Using standard VMC techniques [39,40,44], we then find the ground-state energy as a function of η, shown in Fig. 4(d). The Huse-Elser energies display a remarkable agreement with the LFWT theory, with only a slightly lower energy. We can then argue that LFWT and variational methods provide consistent results for the FM AFOxz energy, which allows the use of E_{LFWT} as the estimator for the ordered state energy.

IV. QUANTUM SPIN-ORBITAL LIQUID AND VALENCE BOND CRYSTALS

In Ref. [36], a QSOL was identified as the best candidate for the ground state of the SU(4) Heisenberg model. Within parton mean-field theory [45], the state can be pictured as four flavors of free fermions hopping in a background with π flux of the emergent gauge field through every hexagon of the lattice. With the constraint of one fermion per site, quarter filling of the bands gives rise to a gapless spectrum with a Dirac dispersion at low energies. Being gapless, such two-dimensional QSOL is, in principle, stable beyond the mean-field level, when gauge fluctuations are included [46].

An important question is whether such QSOL survives in the presence of SU(4)-symmetry-breaking perturbations like the ones considered in model (5). Based on exact diagonalization on small clusters, the authors of Ref. [31] argued for a QSOL phase over an extended region in the parameter space around the SU(4)-symmetric point. In the following, we use VMC methods to investigate the stability of the QSOL in our model. In contrast to ED, the computational time to obtain an observable mean-value and variance with VMC increases polynomially instead of exponentially. Hence, VMC calculations can then be performed in larger samples and allows
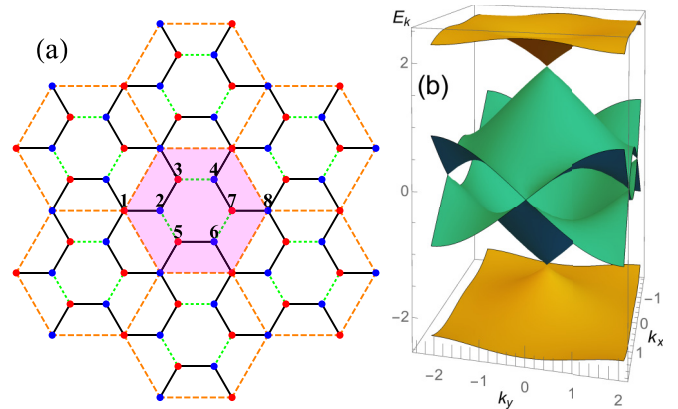

FIG. 5. (a) Mean-field ansatz for the π-flux state. The links in black have $\chi_{ij} = \chi$ ($\phi_{ij} = 0$) while the links in green have $\chi_{ij} = -\chi$ ($\phi_{ij} = \pi$). (b) Dispersion relation of the π-flux state. The parton mean-field ground state is obtained through the occupation of the states in the lowest energy band displayed in yellow.

a more reliable extrapolation to the thermodynamic limit. Moreover, VMC algorithms can be used to study VBC states parting from small modifications of QSOL wave functions, making it an adequate technique to evaluate the energetics of these two classes of states.

A. Quantum spin-orbital liquid

First, we introduce the fermionic parton representation of the SU(4) generators

$$S_a^b(i) = f_{i,a}^\dagger f_{i,b}, \qquad (18)$$

in which $a = 1, \ldots, 4$ labels the color states and i labels the lattice site. The fermionic operators satisfy the canonical relation $\{f_{i,a}, f_{j,b}^\dagger\} = \delta_{ij}\delta_{ab}$ and define a Fock space. Equation (18) is not an exact rewriting of $S_a^b(i)$ since the physical Hilbert space is isomorphic only to the Fock subspace that satisfies the local single-occupancy constraint $\sum_a f_{i,a}^\dagger f_{i,a} = 1$. VMC allows an evaluation of averages for observables after implementing a numerical projection to the physical space.

To generate a trial wave function for the QSOL, we first determine the ground state of the mean-field Hamiltonian

$$\mathcal{H}_{\text{mf}} = -\sum_a \sum_{\langle ij \rangle} [\chi_{ij} f_{i,a}^\dagger f_{j,a} + \text{H.c.}], \qquad (19)$$

where the choice of parameters $\chi_{ij} \in \mathbb{C}$ specify the mean-field ansatz. This ansatz is invariant under SU(4) transformations, thus enforcing a higher symmetry on the state than the SU(2)$\times\mathbb{Z}_3$ symmetry of model (5). Translational invariance requires the absolute value of χ_{ij} to be uniform: $\chi_{ij} = \chi e^{i\phi_{ij}}$, where $\chi > 0$ and ϕ_{ij} is the phase associated with the link $\langle ij \rangle$. The gauge flux Φ on each elementary hexagonal plaquette is defined by $e^{i\Phi} \equiv \prod_{\langle ij \rangle \in \bigcirc} e^{i\phi_{ij}}$. Here we focus on the π-flux state with $\Phi = \pi$ through every hexagon [36] [see Fig. 5(a)]. The corresponding dispersion relation showing a single Dirac cone at the Γ point is illustrated in Fig. 5(b).

The ground state at the mean-field level $|\psi_0\rangle$ is obtained by filling the lower band shown in Fig. 5(b). We just outline the VMC procedure since technical details on how to perform
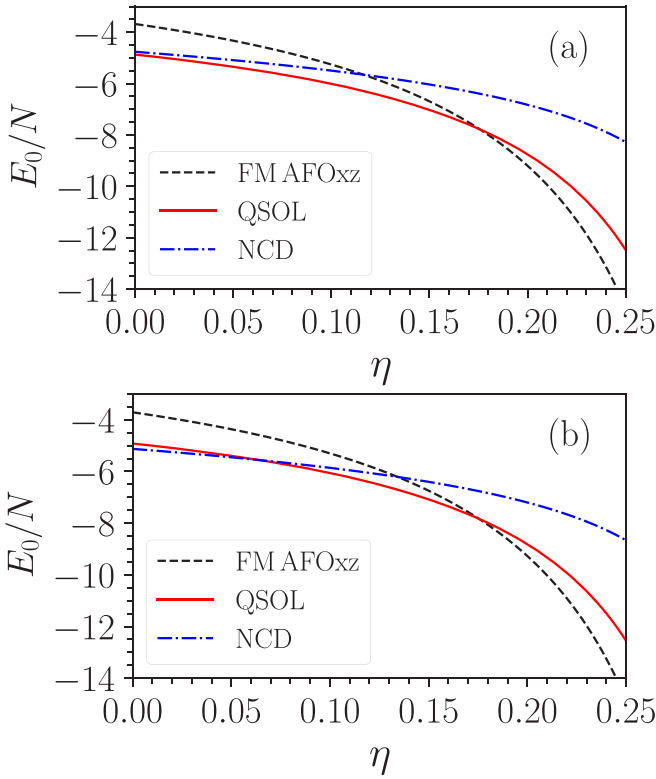
FIG. 6. Comparison of the energy, per site, of three different states: FM AFOxz, QSOL, and NCD (see text) as a function of the Hund's coupling η for (a) $\xi = 0.2$ and (b) $\xi = 0.25$. We identify the phase transitions as the crossing points between the different curves.

the Gutzwiller projection of the mean-field wave functions can be found in the specialized literature [16,20,36,44]. The energy of the Gutzwiller-projected $|\psi_0\rangle$ is calculated for the KK model in Eq. (8) for different values of ξ and η (see Fig. 6). We consider honeycomb lattices of linear length L and $N = 2L^2$ sites with $L = 6$, 12, and 18. An initial state for the Monte Carlo evaluation is chosen by randomly placing each color at $N/4$ sites of our lattice. Our Monte Carlo move consists in exchanging a random pair of sites containing distinct colors, which is accepted or rejected according to the general Metropolis algorithm. A Monte Carlo sweep consists of $\sim 10^3$ exchanges attempts. After every sweep, we compute the ground-state energy E_0. We typically perform $\sim 10^5$ sweeps, with half of the steps discarded for equilibration.

We compared the energy of this particular QSOL to that of the ordered state FM AFOxz. Recall that, as discussed in Sec. III, the AFM AFOxz phase is unstable against quantum fluctuations and disappears completely. We find that the QSOL extends itself away from the SU(4) point, and covers an appreciable portion of the phase diagram before giving room for the FM AFOxz at $\eta \approx 0.175$, a value which is essentially independent of ξ. The presence of the FM AFOxz phase at large η is expected: Hund's coupling favors a ferromagnetic spin alignment, while the local Hubbard repulsion favors a staggered orbital occupation [47]. Nevertheless, the QSOL originally identified in Ref. [36] survives the introduction of a finite Hund's coupling and orbital anisotropy, and it is a
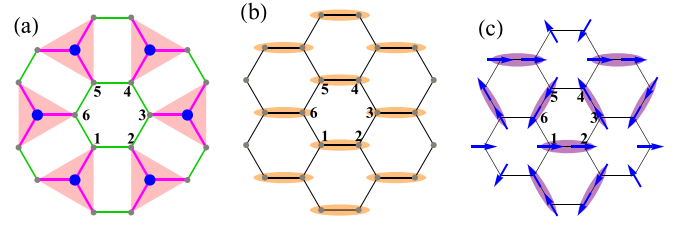

FIG. 7. Valence bond crystal states considered in this work: (a) tetramerized state, in which the sites inside magenta triangles form an SU(4) singlet; (b) dimerized state given by the product of a ferromagnetic order and collinear orbital dimers; (c) product state of noncollinear spin dimers and the ferro-orbital vortex state of Fig. 3(d).

competitive ground state for KK models in the honeycomb lattice.

B. Valence bond crystals

In Sec. IV A, we found that the QSOL is eventually replaced by an ordered state for large enough Hund's coupling η. Now we want to investigate different instabilities of the QSOL, specially as a function of ξ and focused on the formation of VBC states. We start this investigation with the tetramerized state. Here the spins form four-site singlet plaquettes breaking translational symmetry but preserving the SU(4) symmetry [48]. A possible tetramer covering of the honeycomb lattice is illustrated in Fig. 7(a). We tested the stability of the π-flux state against this tetramerization pattern by considering variational wave functions generated by the mean-field Hamiltonian

$$\mathcal{H}_{\text{mf,t}} = \sum_{m=1}^{4} \left[\sum_i \tilde{\varepsilon}_i f_{im}^\dagger f_{im} - \sum_{\langle ij \rangle} (\tilde{\chi}_{ij} f_{im}^\dagger f_{jm} + \text{H.c.}) \right]. \quad (20)$$

Here we keep the π-flux ansatz, so we modulate the sign of $\tilde{\chi}_{ij}$ as in Fig. 5(d), but we also allow for nonuniform magnitude of the mean-field parameters: $|\tilde{\chi}_{ij}| = \chi^{\text{tet}}$ if sites i and j belong to the same tetramer and $|\tilde{\chi}_{ij}| = \chi$ otherwise. Furthermore, we define a negative on-site energy $\tilde{\varepsilon}_i$ for sites at the center of the tetramers [see sites highlighted in Fig. 7(a)]. For $\tilde{\varepsilon}_i = 0$ and $\chi_{ij}^{\text{tet}} = \chi$, we recover the uniform π-flux state. The fully tetramerized state is the product of independent four-site SU(4) singlets throughout the lattice [49]. To quantify the degree of tetramerization of the projected wave functions, we consider the permutation operator between nearest neighbors: $P_{ij} = \sum_{a,b} S_a^b(i) S_b^a(j)$, with the color exchange operators $S_a^b(i)$ defined in Eq. (10). The tetramerization order parameter is defined by [48]

$$r_{\text{tet}} = \frac{4}{5}(P_1 - P_2), \quad (21)$$

where P_1 is the expectation value of P_{ij} for bonds connecting sites inside a tetramer, while P_2 is the average of P_{ij} for any other bond [Fig. 7(a)]. The parameter $r_{\text{tet}}(\tilde{\varepsilon}, \tilde{\chi})$ is normalized such that $r_{\text{tet}} = 1$ in the four-site plaquette product state. For each value of $\tilde{\varepsilon}$, we select the value of $\tilde{\chi} = \tilde{\chi}_{\min}(\tilde{\varepsilon})$ that gives the lowest energy within VMC and compute the corresponding tetramerization order parameter $r_{\text{tet}}[\tilde{\varepsilon}, \tilde{\chi}_{\min}(\tilde{\varepsilon})]$. Our VMC results in Fig. 8(a) illustrate that the lowest energy is obtained
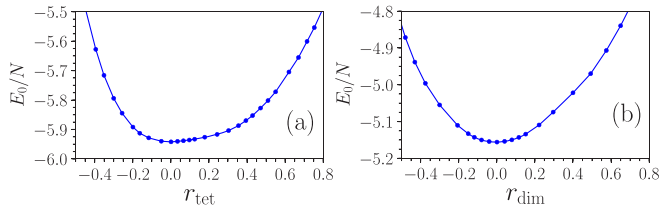
FIG. 8. (a) Ground-state energy of the tetramerized state, per site, as a function of the tetramerization parameter r_{tet}. (b) Ground-state energy of the dimerized state, per site, as a function of the dimerization parameter r_{dim}. We considered $\xi = \eta = 0.1$ for both curves.

for $r_{\mathrm{tet}} = 0$ and thus the uniform state is always selected in the region where the QSOL is stable. This implies that the QSOL is stable against tetramerization, in accordance with the results of Ref. [48] at the SU(4) point.

Next, we consider valence bond crystals constructed after a mean-field decoupling of spin and orbital degrees of freedom [31]. Since it neglects spin-orbital entanglement, this approximation should break down close to the SU(4) point. Nevertheless, it allows us to search for other trial states which may be stable, for instance, in the region $\xi \sim 1$.

As a first example, we consider that the spins are fully polarized while the orbitals form the collinear dimer pattern shown in Fig. 7(b). A simple product state of orbital dimers produces the following ground state energy: $E_0/N = -3(1 + \xi^2)J_1$. It is interesting that this energy improves as one moves away from the SU(4) point, in accordance with our general discussion. We also performed a full VMC study with a mean-field Hamiltonian similar to the one in Eq. (20). The dimerization order parameter is $r_{\mathrm{dim}} = \tilde{P}_1 - \tilde{P}_2$, with $\tilde{P}_1$ the average value of the *two-color* permutation operator on bonds forming a dimer, and $\tilde{P}_2$ is the average value for any other bond. By definition, $r_{\mathrm{dim}} = 1$ in the product state discussed previously. Our VMC results in Fig. 8(b) highlight that the lowest energy occurs for $r_{\mathrm{dim}} = 0$ and thus this orbital dimerization is never favored. Moreover, the overall energy is not competitive and this state does not appear in the phase diagram.

Now we assume that the spins dimerize, while the orbitals develop some type of classical order. A spin dimer is clearly not favored by Hund's coupling and is most likely to be present at small η. In this limit, a reasonable guess for the orbital dependence would be that orbitals belonging to a spin dimer are parallel. However, ferro-orbital order is too high in energy in the region $t' \lesssim t$. Another more promising choice is the ferro-orbital vortex state in Fig. 3(d), coupled to a "Kekule" arrangement of nearest-neighbor spin dimers [50]. The resulting spin-orbital state is depicted in Fig. 7(c). We follow the nomenclature of Ref. [31] and refer to it as a non-collinear spin dimers (NCD) phase. To test this state within VMC, we assume ferro-orbital vortex order and perform a VMC calculation in the resulting spin Hamiltonian allowing for spin dimerization, following the same approach as described above. We now find $r_{\mathrm{dim}} \neq 0$ in the NCD state. Importantly, this is the best variational state in the region $\xi \gtrsim 0.2$ and $\eta \lesssim 0.2$, as indicated by Fig. 6. The detailed comparison of the energies of the variational states FM AFOxz, QSOL,

and NCD leads to the phase diagram in Fig. 1. However, we find no competitive candidate, within VMC, for the LFWT unstable region in Fig. 1. In particular, we investigated states with partially polarized spins, following the suggestion of the authors of Ref. [31], but their energy is never competitive [see, for instance, Fig. 8(b)].

V. DISCUSSION

We revisited a Kugel-Khomskii model in the honeycomb lattice previously studied in the context of spin-orbital physics of $Ba_3CuSb_2O_9$ and quarter-filled twisted bilayer graphene [24,31]. This model contains an SU(4)-symmetric point at which a QSOL phase may be realized [36]. Using a combination of analytical and numerical techniques, we found that this QSOL covers an extended parameter regime in the phase diagram where we include the effects of Hund's coupling and bond-dependent frustrated exchange interactions. This result raises hopes that a QSOL state may be observed in honeycomb lattice materials with active spin and orbital degrees of freedom.

$Ba_3CuSb_2O_9$ contains Cu^{2+} ions with a $3d^9$ configuration. In a first approximation, one may assume that this hole has a fourfold degeneracy: a twofold spin degeneracy and a twofold orbital degeneracy of the e_g orbitals. Normally, one would expect this degeneracy to be lifted and long-range order to develop for both spin and orbital degrees of freedom at low temperatures. However, no spin freezing is detected down to 20 mK [51], considerably below the Curie-Weiss temperature of 50 K, and no evidence for a cooperative Jahn-Teller effect is found down to 12 K [37,52]. These experimental observations motivated the proposal of this material as a QSOL candidate [37,51]. Nevertheless, as stressed by Ref. [31], the microscopic model in Eq. (5) is too simplistic to describe $Ba_3CuSb_2O_9$ and a QSOL is likely not its ground state. For this material, a more realistic Hamiltonian on a decorated honeycomb lattice should be taken into account.

In TBG, the orbital degrees of freedom originate from the two Dirac points in the original Brillouin zone of each graphene sheet, which should be centered on a honeycomb superlattice due to symmetry constraints [53–55]. The effective Hamiltonian obtained at quarter filling is the SU(4) Heisenberg model [24]. As we increase the Hund's coupling, we find long-range ferromagnetic order in the spins and antiferromagnetic order in the orbitals, providing a possible connection with a recently found spin-polarized state [56–58]. While longer-range exchange couplings are likely to be relevant in the Mott insulating phase of TBG [50,59], an intriguing possibility is that a spin-polarized phase exists in proximity to a QSOL [60] in this highly tunable system.

We close this paper with remarks about three solid-state platforms that would be described by similar KK models: the trilayer graphene/hexagonal boron nitride heterostructures (TLG/hBN) [27–30], the tiny-angle TBG system [61], and the $j = 3/2$ compound α-ZrCl$_3$ [19]. KK models for TLG/hBN also display twofold orbital degeneracy, but these Wannier orbitals are located on a triangular lattice, which implies that our results are not extendable to this system. However, our methodology is undoubtedly applicable to these models and can provide complementary results. The same

comment applies to the tiny-angle TBG under an electric field, which is possibly described by a KK model on an emergent kagome lattice [61]. Concerning the layered honeycomb material α-ZrCl$_3$, it is expected that extended versions of the minimal model derived in Refs. [19,20] would lead to exchange frustration similar to the ones discussed in this paper. The phase diagram of a realistic model for this compound would then present extended regions of stability for the QSOL and the NCD phases, with possible connection with α-ZrCl$_3$ magnetism.

[1] K. I. Kugel and D. I. Khomskii, Sov. Phys. Usp. **25**, 231 (1982).

[2] M. Imada, A. Fujimori, and Y. Tokura, Rev. Mod. Phys. **70**, 1039 (1998).

[3] Y. Tokura and N. Nagaosa, Science **288**, 462 (2000).

[4] G. Khaliullin, Prog. Theor. Phys. Suppl. **160**, 155 (2005).

[5] F. Krüger, S. Kumar, J. Zaanen, and J. van den Brink, Phys. Rev. B **79**, 054504 (2009).

[6] X. Dou, V. N. Kotov, and B. Uchoa, Sci. Rep. **6**, 31737 (2016).

[7] H. Ueda, T. Morimoto, and T. Momoi, Phys. Rev. B **98**, 045128 (2018).

[8] L. F. Feiner, A. M. Olés, and J. Zaanen, Phys. Rev. Lett. **78**, 2799 (1997).

[9] Z. Nussinov and J. van den Brink, Rev. Mod. Phys. **87**, 1 (2015).

[10] F. Reynaud, D. Mertz, F. Celestini, J.-M. Debierre, A. M. Ghorayeb, P. Simon, A. Stepanov, J. Voiron, and C. Delmas, Phys. Rev. Lett. **86**, 3638 (2001).

[11] M. V. Mostovoy and D. I. Khomskii, Phys. Rev. Lett. **89**, 227203 (2002).

[12] K. Penc, M. Mambrini, P. Fazekas, and F. Mila, Phys. Rev. B **68**, 012408 (2003).

[13] F. Vernay, K. Penc, P. Fazekas, and F. Mila, Phys. Rev. B **70**, 014428 (2004).

[14] A. J. W. Reitsma, L. F. Feiner, and A. M. Oleś, New J. Phys. **7**, 121 (2005).

[15] G. Chen, R. Pereira, and L. Balents, Phys. Rev. B **82**, 174440 (2010).

[16] W. M. H. Natori, E. C. Andrade, E. Miranda, and R. G. Pereira, Phys. Rev. Lett. **117**, 017204 (2016).

[17] J. Romhányi, L. Balents, and G. Jackeli, Phys. Rev. Lett. **118**, 217202 (2017).

[18] W. M. H. Natori, M. Daghofer, and R. G. Pereira, Phys. Rev. B **96**, 125109 (2017).

[19] M. G. Yamada, M. Oshikawa, and G. Jackeli, Phys. Rev. Lett. **121**, 097201 (2018).

[20] W. M. H. Natori, E. C. Andrade, and R. G. Pereira, Phys. Rev. B **98**, 195113 (2018).

[21] Y. Cao, V. Fatemi, S. Fang, K. Watanabe, T. Taniguchi, E. Kaxiras, and P. Jarillo-Herrero, Nature **556**, 43 (2018).

[22] Y. Cao, V. Fatemi, A. Demir, S. Fang, S. L. Tomarken, J. Y. Luo, J. D. Sanchez-Yamagishi, K. Watanabe, T. Taniguchi, E. Kaxiras, R. C. Ashoori, and P. Jarillo-Herrero, Nature **556**, 80 (2018).

[23] C. Xu and L. Balents, Phys. Rev. Lett. **121**, 087001 (2018).

[24] J. W. F. Venderbos and R. M. Fernandes, Phys. Rev. B **98**, 245103 (2018).

[25] N. F. Q. Yuan and L. Fu, Phys. Rev. B **98**, 045103 (2018).

[26] Y.-H. Zhang and T. Senthil, Phys. Rev. B **99**, 205150 (2019).

[27] L. Classen, C. Honerkamp, and M. M. Scherer, Phys. Rev. B **99**, 195120 (2019).

[28] C. Schrade and L. Fu, Phys. Rev. B **100**, 035413 (2019).

[29] X.-C. Wu, A. Keselman, C.-M. Jian, K. A. Pawlak, and C. Xu, Phys. Rev. B **100**, 024421 (2019).

[30] Y.-H. Zhang and D. Mao, arXiv:1906.10132.

[31] A. Smerald and F. Mila, Phys. Rev. B **90**, 094422 (2014).

[32] K. I. Kugel, D. I. Khomskii, A. O. Sboychakov, and S. V. Streltsov, Phys. Rev. B **91**, 155125 (2015).

[33] I. Affleck and J. B. Marston, Phys. Rev. B **37**, 3774 (1988).

[34] D. P. Arovas and A. Auerbach, Phys. Rev. B **38**, 316 (1988).

[35] N. Read and S. Sachdev, Phys. Rev. Lett. **66**, 1773 (1991).

[36] P. Corboz, M. Lajkó, A. M. Läuchli, K. Penc, and F. Mila, Phys. Rev. X **2**, 041013 (2012).

[37] S. Nakatsuji, K. Kuga, K. Kimura, R. Satake, N. Katayama, E. Nishibori, H. Sawa, R. Ishii, M. Hagiwara, F. Bridges, T. U. Ito, W. Higemoto, Y. Karaki, M. Halim, A. A. Nugroho, J. A. Rodriguez-Rivera, M. A. Green, and C. Broholm, Science **336**, 559 (2012).

[38] J. Nasu and S. Ishihara, Phys. Rev. B **88**, 094408 (2013).

[39] D. A. Huse and V. Elser, Phys. Rev. Lett. **60**, 2531 (1988).

[40] F. Ferrari, S. Bieri, and F. Becca, Phys. Rev. B **96**, 104401 (2017).

[41] C. Wu, Phys. Rev. Lett. **100**, 200406 (2008).

[42] A. Joshi, M. Ma, F. Mila, D. N. Shi, and F. C. Zhang, Phys. Rev. B **60**, 6584 (1999).

[43] J. Chaloupka and G. Khaliullin, Phys. Rev. B **92**, 024413 (2015).

[44] C. Gros, Ann. Phys. (NY) **189**, 53 (1989).

[45] L. Savary and L. Balents, Rep. Prog. Phys. **80**, 016502 (2017).

[46] M. Hermele, T. Senthil, M. P. A. Fisher, P. A. Lee, N. Nagaosa, and X.-G. Wen, Phys. Rev. B **70**, 214437 (2004).

[47] D. Khomskii, *Transition Metal Compounds* (Cambridge University Press, Cambridge, England, 2014).

[48] M. Lajkó and K. Penc, Phys. Rev. B **87**, 224428 (2013).

[49] Y. Q. Li, M. Ma, D. N. Shi, and F. C. Zhang, Phys. Rev. Lett. **81**, 3527 (1998).

[50] X. Y. Xu, K. T. Law, and P. A. Lee, Phys. Rev. B **98**, 121406(R) (2018).

[51] J. A. Quilliam, F. Bert, E. Kermarrec, C. Payen, C. Guillot-Deudon, P. Bonville, C. Baines, H. Luetkens, and P. Mendels, Phys. Rev. Lett. **109**, 117203 (2012).

[52] N. Katayama, K. Kimura, Y. Han, J. Nasu, N. Drichko, Y. Nakanishi, M. Halim, Y. Ishiguro, R. Satake, E. Nishibori, M.

Yoshizawa, T. Nakano, Y. Nozue, Y. Wakabayashi, S. Ishihara, M. Hagiwara, H. Sawa, and S. Nakatsuji, Proc. Natl. Acad. Sci. USA **112**, 9305 (2015).

[53] J. Kang and O. Vafek, Phys. Rev. X **8**, 031088 (2018).

[54] M. Koshino, N. F. Q. Yuan, T. Koretsune, M. Ochi, K. Kuroki, and L. Fu, Phys. Rev. X **8**, 031087 (2018).

[55] H. C. Po, L. Zou, A. Vishwanath, and T. Senthil, Phys. Rev. X **8**, 031089 (2018).

[56] K. Seo, V. N. Kotov, and B. Uchoa, Phys. Rev. Lett. **122**, 246402 (2019).

[57] A. L. Sharpe, E. J. Fox, A. W. Barnard, J. Finney, K. Watanabe, T. Taniguchi, M. A. Kastner, and D. Goldhaber-Gordon, Science **365**, 605 (2019).

[58] M. Serlin, C. L. Tschirhart, H. Polshyn, Y. Zhang, J. Zhu, K. Watanabe, T. Taniguchi, L. Balents, and A. F. Young, arXiv:1907.00261.

[59] J. Kang and O. Vafek, Phys. Rev. Lett. **122**, 246401 (2019).

[60] D. Kiese, F. Lasse Buessen, C. Hickey, S. Trebst, and M. M. Scherer, arXiv:1907.09490.

[61] A. Ramires and J. L. Lado, Phys. Rev. Lett. **121**, 146801 (2018).